analytical chemistry

pubs.acs.org/ac Article

In Situ Visualization of Epidermal Growth Factor Receptor Nuclear Translocation with Circular Bivalent Aptamer

Lei Zhang, Mengge Chu, Cailing Ji, Junyuan Wei, Yanbing Yang, Zhongnan Huang, Weihong Tan, Jie Tan,* and Quan Yuan

Cite This: https://doi.org/10.1021/acs.analchem.2c02762 Read Online

ACCESS | Metrics & More | Article Recommendations | Supporting Information

ABSTRACT: Epidermal growth factor receptor (EGFR) nuclear translocation correlates with the abnormal proliferation, migration, and anti-apoptosis of tumor cells. Monitoring EGFR nuclear translocation provides insights into the molecular mechanisms underlying cancers. EGFR nuclear translocation includes two processes, EGFR phosphorylation and phosphorylated EGFR translocation to the nucleus. With the help of aptamers, probes that can achieve the first step of anchoring phosphorylated EGFR have been developed. However, the EGFR nuclear translocation can last for hours, posing a challenge to monitor the entire nuclear translocation in living cells. Herein, we designed a circular bivalent aptamer-functionalized optical probe with greatly enhanced stability for long-term visualization of EGFR nuclear translocation in situ. The results of cell experiments show that the probe could monitor the entire nuclear translocation of EGFR. The findings of tissue and *in vivo* experiments demonstrate that the probe can evaluate the development and progression of tumors by imaging EGFR nuclear translocation in situ. The proposed approach allows us to monitor EGFR nuclear translocation in the long term, indicating its great potential in investigating the mechanisms of cancers and guiding for tumor treatment.

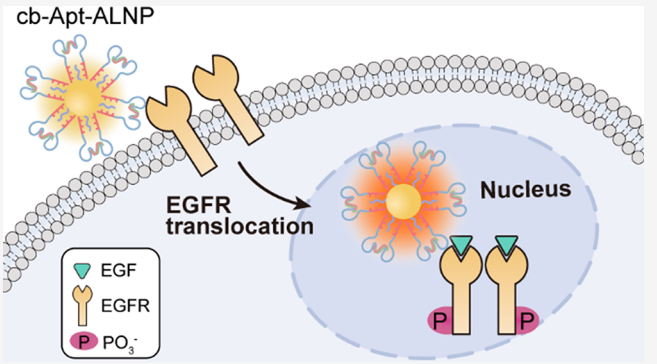

INTRODUCTION

Protein nuclear translocation represents the movement of proteins from the cytoplasm to the nucleus.[1] During this process, certain proteins enter the cell nucleus to control gene expression and regulate cellular function.[2,3] It has been reported that the protein nuclear translocation of the epidermal growth factor receptor (denoted as EGFR) is closely related to the development of cancers.[4,5] Specifically, when EGFR binds to its ligand epidermal growth factor (denoted as EGF), EGFR undergoes autophosphorylation and translocates to the nucleus to exert kinase activity, thus activating downstream signaling pathways.[6−8] Dynamic translocation processes of EGFR are correlated with the abnormal proliferation, migration, and anti-apoptosis of tumor cells.[9,10] Therefore, exploring EGFR nuclear translocation is critical for understanding the molecular mechanism of cancers and could be further applied to potential areas such as tumor status evaluation.

An ideal strategy for imaging EGFR nuclear translocation would first anchor phosphorylated EGFR and should allow the observation of the entire process of EGFR nuclear translocation in living cells. Molecular recognition probes such as antibodies,[11] ligands,[12] or aptamers[13,14] have been proposed for EGFR localization. Among them, aptamers are labeled with accurate dye stoichiometry and have been utilized for quantitative nanoscale imaging,[15,16] providing a solution for precise observation of EGFR nuclear translocation. However, the nuclear translocation process of proteins can be as long as several hours.[17,18] Aptamer-based probes are often easy to be degraded,[19,20] posing a challenge for in situ monitoring the entire nuclear translocation in living cells.

Circular bivalent aptamer (cb-Apt) with fixed ends can eliminate the major source of degradation,[21] providing an effective and straightforward strategy for improving the long-term stability of the entire probe. Herein, a circular bivalent aptamer-functionalized optical probe (denoted as cb-Apt-ALNP) was rationally designed. The cb-Apt in the probe could accurately anchor phosphorylated EGFR on the cell membrane. Then, the optical signal changes of the probe were monitored, allowing us to continuously and in situ visualize the process of EGFR nuclear translocation in living cells (Scheme 1). In complex biological environments, we found that the cb-Apt endows the probe with good stability and can anchor

Received: June 27, 2022
Accepted: November 10, 2022

https://doi.org/10.1021/acs.analchem.2c02762
Anal. Chem. XXXX, XXX, XXX−XXX

Scheme 1. Principle of cb-Apt-ALNP for EGFR Nuclear Translocation Detection

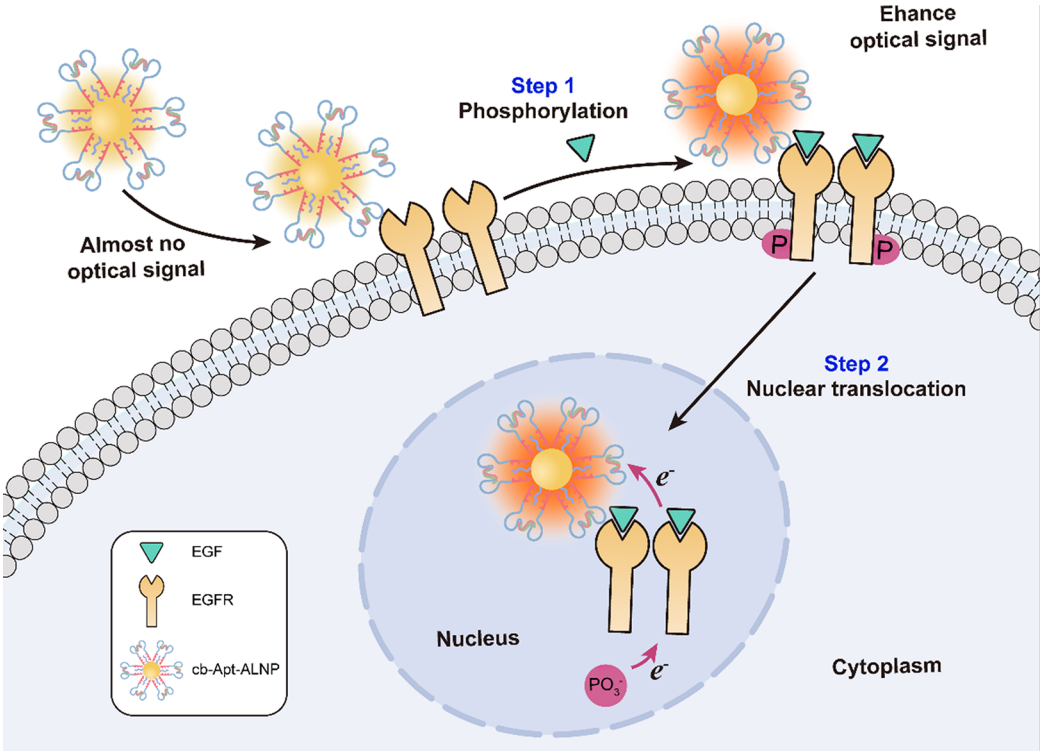

phosphorylated EGFR for a long time. This property lays the foundation for the probe to monitor the protein nuclear translocation for up to several hours. Overall, this approach not only helps in revealing the process of EGFR nuclear translocation in living cells but also provides insights into the progression of cancers and guidance for tumor treatment.

MATERIALS AND METHODS

Reagents and Materials. All DNA synthesis reagents were obtained from Glen Research (Sterling; VA), and the Protected Fe base was synthesized in our lab. Fetal bovine serum (FBS) was purchased from Zeta life. Dulbecco's phosphate buffered saline (DPBS; Gibco), RPMI-1640 medium (Gibco), and Dulbecco's modified Eagle medium (DMEM; Gibco) were obtained from Thermo Fisher Scientific Inc. Epidermal growth factor (EGF) was purchased from Abcam. Bovine serum albumin (BSA) was obtained from Beyotime. Deionized (DI) water (resistivity ~18.2 MΩ·cm) was used throughout the experiments.

Construction of Circular Bivalent Aptamer (cb-Apt). To prepare cb-Apt, its two components (S13-1 and S13-2) were first dissolved in binding buffer in an appropriate concentration and then heated at 95 °C for 5 min, followed by quick cooling to 4 °C, allowing the formation of cb-Apt.

Preparation of Apt-ALNPs and Cb-Apt-ALNPs. The ferrocene nucleotide modified DNA oligonucleotide was attached to nanoparticles via the hydrophobic interaction. In short, 2 mg of ALNPs were dispersed in toluene. Then, 3 nmol of single-stranded or cb-Apt was dissolved in 1 mL of sterile water and added to the above solution under vigorous stirring. Subsequently, ALNPs were transferred from the upper toluene phase to the lower water phase, and the water solution was transferred to a centrifuge tube. The obtained Apt-ALNPs or cb-Apt-ALNPs were collected by centrifugation and finally dispersed in sterile water.

Cell Culture. A549 cells, L02 cells, and CAL-27 cells were derived from China Center for Type Culture Collection (CCTCC). A549 cells were cultured in RPMI 1640 medium supplemented with 10% FBS. L02 cells and CAL-27 cells were cultivated in DMEM medium supplemented with 10% FBS. The cells were maintained at 37 °C in a humidified atmosphere containing 5% CO_2.

***Z*-Axis Scanning.** A549 or L02 cells were seeded in 20 mm of confocal dishes at a density of 5×10^4 per well and incubated overnight. Cells were then incubated with cb-Apt-ALNPs (75 $\mu g \cdot mL^{-1}$) at 37 °C for 30 min. Subsequently, cells were cultured in solution without or with EGF (100 $ng \cdot mL^{-1}$) at 37 °C for 10 min. The cells were washed and visualized by confocal microscopy. Micrographs were taken per 0.39 μm while moving the focal plane in incremental steps from the dish bottom up to the top of the cells.

Cell Migration Assay. The 6-well plates were respectively plated with 4×10^5 A549 cells and L02 cells. The cells were grown to confluence before beginning the experiment. A scratch was created with a 100 μL pipette tip, after which a new serum-free medium without or with 100 nM EGF was added and monitored for 48 h following the start of the experiment. The closure degree of the scratched area was expressed as a percentage of the initial scratched area. At 0, 12, 24, 36, and 48 h, pictures of the wounds at three different locations were taken. The wounds were quantitatively measured, and the remaining wound areas were calculated using ImageJ software.

Three-Dimensional Multicellular Spheroids (MCSs). For A549 or L02 multicellular spheroids generation, cell suspensions of 100 μL per well at optimized densities (1×10^3 $cells \cdot mL^{-1}$) were dispensed into 96-well U-plates (MS-9096UZ, Japan). Plates were incubated for 5 days at 37 °C

https://doi.org/10.1021/acs.analchem.2c02762
Anal. Chem. XXXX, XXX, XXX−XXX

in a humidified 5% CO_2 atmosphere. Then, the culture medium was replaced with DPBS mixed with EGF and cocultured for 10 min. Subsequently, multicellular spheroids were incubated with cb-Apt-ALNPs (75 $\mu g \cdot mL^{-1}$) in DPBS for 30 min. After that, Z-stack images of the spheroids were acquired at 5 μm intervals using a confocal microscope (TI-E A1RMP N-STORM, Nikon) equipped with a CCD camera.

***In Vivo* Imaging.** All animal studies were performed in accordance with protocols approved by Hunan University Laboratory Animal Center, and all mice received humane care in compliance with the Guide for the Care and Use of Laboratory Animals. All mice had access to food and water ad libitum. Five-week-old female athymic BALB/c nude mice received a subcutaneous injection of 7×10^6 A549 cells into the right backside. When tumor volume reached 70 mm^3, various materials were injected intravenously via the tail vein (30 μL). After the mice were anesthetized with isopentane, *in vivo* imaging was performed.

RESULTS AND DISCUSSION

Synthesis and Characterization of Cb-Apt-ALNPs. The cb-Apt-ALNP consists of two parts, a circular bivalent aptamer (denoted as cb-Apt) and an alkylated afterglow luminescent nanoparticle (denoted as ALNP). Taking the EGFR-targeting aptamer S13[22] as the main part, additional flanking complementary sequences were added and ferrocene nucleotides[23] with strong hydrophobicity were modified (Figures S1–S6 and Table S1). The cb-Apt was formed by hybridization of additional complementary sequences. The alkylated ALNP was synthesized using a hydrothermal method as described in our previous work (Figure S7).[24] The strong hydrophobic interaction between alkylated ALNP and cb-Apt was conducive to forming cb-Apt-ALNP (Figure 1a).[25,26] The cb-Apt was selected as a recognition unit to specifically anchor EGFR. ALNP was chosen as the signal unit since its afterglow signal could be significantly affected by electron transfer in phosphorylation.[27,28] To be specific, there are holes and free electrons stored in the energy traps of ALNPs. When the excitation light is removed, holes or free electrons are released from energy traps with afterglow luminescence. The increase in the number of electrons could improve the recombination probability of electrons and holes, thereby enhancing afterglow luminescence.[29−31] The electrons transferred during the EGFR phosphorylation reaction can flow to the ALNPs and change their electron distribution, enhancing the signal of ALNPs.[27]

The synthesis of cb-Apt was verified by agarose gel electrophoresis as the cb-Apt obviously retarded its migration compared to single-stranded components (Figure 1b). The effects of cyclization on cb-Apt stability in different biological media were also investigated. The band integrity of cb-Apt was still evident after incubation with serum for 8 h, while the band of single DNA was degraded after 1 h incubation (Figure 1c and Figure S8). The cb-Apt could retain sequence integrity even after incubating with exonuclease I (Exo I) for 12 h (Figure S9). Based on stability analysis of aptamers treated with serum and Exo I, it can be concluded that the cyclization of aptamer improves stability in complex biological environments. The stability of the single-stranded aptamer is mainly limited by its free ends, which are easily recognized and cleaved by exonucleases.[32] Also, the free ends of single-stranded aptamers are prone to unnecessary DNA rearrangements.[33] Compared with the linear aptamer, circular structures possess better thermal stability and higher conformational

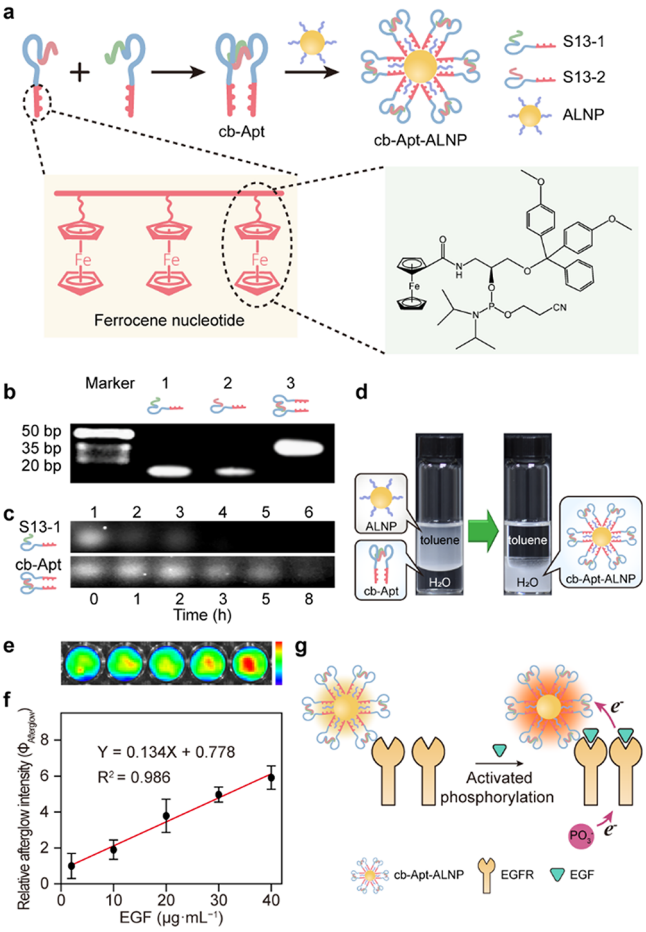

Figure 1. Synthesis, characterization, and responsiveness of cb-Apt-ALNPs. (a) Schematic of the synthesis process of cb-Apt-ALNPs. (b) Agarose gel electrophoresis revealed the formation of cb-Apt. The cb-Apt (lane 3) was prepared with S13-1 (lane 1) and S13-2 (lane 2). (c) Agarose gel electrophoresis was employed to analyze the stability of cb-Apt after incubating with 10% FBS for 0, 1, 2, 3, 5, and 8 h (lane 1−lane 6). (d) Schematic of the phase transfer process. (e) Corresponding pseudo-color image of cb-Apt-ALNPs after being incubated at various EGF concentrations. A representative image of three biologically independent samples from each group is shown. Color bar: 4.97×10^5−4.77×10^6. (f) Dose-dependent afterglow intensity of cb-Apt-ALNPs after being incubated in PBS at various EGF concentrations. Data are presented as the mean ± standard deviation. $n = 3$. (g) Schematic of cb-Apt-ALNPs for EGFR phosphorylation imaging (not to scale).

stability due to lack of free ends and reduced misfolding.[34,35] In addition, cb-Apt not only enhanced binding affinity but also doubled the internalization of single strand (Figures S10–S12), making cb-Apt much more suitable as a candidate for EGFR nuclear translocation detection. In the phase transfer reaction, it was clearly observed that the ALNPs were transferred from the oil phase to the water phase, implying that the cb-Apt was modified on the ALNPs (Figure 1d). After quantitative analysis, cb-Apt was efficiently modified onto ALNPs with about 85% yield (Figure S13 and Table S2). Transmission electron microscopy, dynamic light scattering, elemental mapping images, and statistical size distributions all clearly demonstrated the successful construction of the cb-Apt-ALNPs (Figures S14–S16). The excitation, emission, and absorption spectra of cb-Apt-ALNPs were characterized (Figures S17–S19). This proved the synthesis of cb-Apt-

https://doi.org/10.1021/acs.analchem.2c02762
Anal. Chem. XXXX, XXX, XXX−XXX

ALNPs, and the optical properties were not affected by cb-Apt modification. The colocalization experiments *in vitro* and *in vivo* were conducted, demonstrating the EGFR targeting of cb-Apt (Figures S20 and S21).

Responsiveness of Cb-Apt-ALNPs to EGFR Phosphorylation. *In vitro* experiments were performed to explore whether the afterglow signal of cb-Apt-ALNPs varies with EGFR phosphorylation. Before this, the cytotoxicity of cb-Apt-ALNPs was evaluated using the CCK-8 assay. Statistically, the viability of A549 cells was still higher than 90% after 24 h incubation with cb-Apt-ALNPs. As a result, cb-Apt-ALNPs were well tolerant and have low toxicity *in vitro* (Figure S22). As a ligand of EGFR, EGF was used to activate the EGFR phosphorylation. A549 lung cancer cells were chosen as the model cell due to their high EGFR expression.[36] Based on this, A549 cells were incubated with varying concentrations of EGF to trigger cellular EGFR phosphorylation. As shown in the pseudo-color image of afterglow, the afterglow signals of cb-Apt-ALNPs increase continuously with the addition of EGF (Figure 1e). The relation between afterglow intensity and the addition of EGF was analyzed to evaluate whether cb-Apt-ALNPs can characterize EGFR phosphorylation. Relative afterglow intensity ($\Phi_{Afterglow}$) was defined as the ratio of afterglow intensity change to initial afterglow intensity.[37] The formula was listed as follows:

$$\Phi_{Afterglow} = (I_f - I_o)/I_o \quad (1)$$

where I_o is defined as the original afterglow intensity, which means the afterglow intensity before a given stimulus, and I_f is the afterglow intensity after stimulation. Afterglow intensity (I) is determined by the excitation source, excitation time, number of nanoparticles, and luminous efficiency of nanoparticles.[38] Under the same excitation conditions, the afterglow intensity is directly proportional to the luminous efficiency (Q) and the number of nanoparticles (N):

$$I \propto Q \times N \quad (2)$$

By combining formulas 1 and 2

$$\Phi_{Afterglow} \propto (Q_f \times N - Q_o \times N)/(Q_o \times N)$$
$$\propto (Q_f - Q_o)/Q_o \quad (3)$$

where Q_o represents the original luminous efficiency, which means the luminous efficiency before a given stimulus, and Q_f is the luminous efficiency after stimulation. From formula 3, it is found that the $\Phi_{Afterglow}$ is not affected by the number of nanoparticles and is related to the luminous efficiency of nanoparticles. The luminous efficiency of nanoparticles is influenced by EGFR phosphorylation; $\Phi_{Afterglow}$ could thus be used to detect the status of EGFR phosphorylation. The calculated $\Phi_{Afterglow}$ of cb-Apt-ALNPs was linearly correlated with the addition of EGF (Figure 1f and Table S3), elucidating that $\Phi_{Afterglow}$ of cb-Apt-ALNPs was positively correlated with EGFR phosphorylation. The Western blot (WB) assay was performed to show the expression of cell phosphorylation under EGF stimulation. The results displayed strong bands for phosphorylated EGFR (pEGFR) with the addition of EGF (Figure S23), verifying that EGFR phosphorylation can be activated effectively by EGF. The results were consistent with the observations of afterglow signals, proving that EGF-activated EGFR phosphorylation can be characterized using the cb-Apt-ALNPs (Figure 1g). Furthermore, cb-Apt-ALNPs maintained a clear response to EGF-activated phosphorylation in complex biological environments. The afterglow images were also acquired by the IVIS Lumina XR Imaging System, and the corresponding calculated $\Phi_{Afterglow}$ exhibited that cb-Apt-ALNPs have two-fold signal enhancement in the presence of EGF (Figures S24 and S25). Taken together, the $\Phi_{Afterglow}$ of cb-Apt-ALNPs positively correlated with EGFR phosphorylation, providing a method for acquiring dynamic information about EGFR nuclear translocation.

Monitoring of Nuclear Translocation by Cb-Apt-ALNPs. In a normal state, EGFR remains in the cell membrane.[39] By binding with external EGF, EGFR is activated to enter the nucleus and trigger downstream signaling events.[40] To explore the detection performance of cb-Apt-ALNPs on EGFR nuclear translocation, the imaging of ALNPs, Apt-ALNPs and cb-Apt-ALNPs in different biological environments was investigated. Bovine serum albumin (BSA) was chosen to simulate the abundant proteins in biological systems,[41] and the long-term stability of the probe for nuclear translocation imaging was evaluated in PBS. A549 cells were separately incubated with ALNPs, Apt-ALNPs, and cb-Apt-ALNPs under different conditions, and afterglow images were obtained by laser scanning confocal microscopy. Nuclear translocation was monitored over a period of up to 1.5 h. The afterglow decay analyses were performed and showed that the luminescence of cb-Apt-ALNPs lasted for more than 60 min (Figure S26). In the absence of BSA, it was found that the afterglow signals of Apt-ALNPs and cb-Apt-ALNPs both increased apparently with the addition of EGF. Notably, cb-Apt-ALNPs had the strongest afterglow signal in the nucleus that represented enhanced EGFR nuclear translocation compared to cells not treated with EGF. This result illustrated that EGF-enhanced nuclear translocation in A549 cells can be clearly monitored by cb-Apt-ALNPs. In the presence of BSA, relative to ALNPs and Apt-ALNPs, the afterglow signal of cb-Apt-ALNPs altered significantly in A549 cells before and after adding EGF (Figure 2a and Figures S27 and S28). The observation indicated that cb-Apt-ALNPs can highly respond to EGFR nuclear translocation even with abundant BSA, which may be attributed to the high affinity and high stability of cb-Apt on the probe. The relative integral optical density (IOD) of these images was calculated. In BSA-treated cells, the IOD of cb-Apt-ALNPs greatly rose from 50 to 100% with the addition of EGF, while ALNPs and Apt-ALNPs showed almost no response (Figure 2b), further implying that EGFR nuclear translocation detection using cb-Apt-ALNPs was hardly affected by proteins in biological environments. In addition, WB was performed to determine the EGFR phosphorylation status. It was found that the EGF stimulation apparently increased the expression of pEGFR (Figure 2c and Figure S29), firmly validating that the alterations of afterglow signals reflect the phosphorylation status.

On this basis, to further evaluate the potential practical applications of cb-Apt-ALNPs, the capacity of cb-Apt-ALNPs on monitoring EGFR nuclear translocation was tested in a complex serum environment. It was observed that the luminescence of cb-Apt-ALNPs in the nucleus remarkably enhanced after EGF treatment, while ALNPs and Apt-ALNPs showed negligible signal change (Figure 2d and Figure S30). The statistical results indicated that the relative IOD values of ALNPs and Apt-ALNPs remained almost the same before and after EGF stimulation. For cb-Apt-ALNPs, the IOD in EGF stimulated group was about two folds higher than that of the

https://doi.org/10.1021/acs.analchem.2c02762
Anal. Chem. XXXX, XXX, XXX−XXX

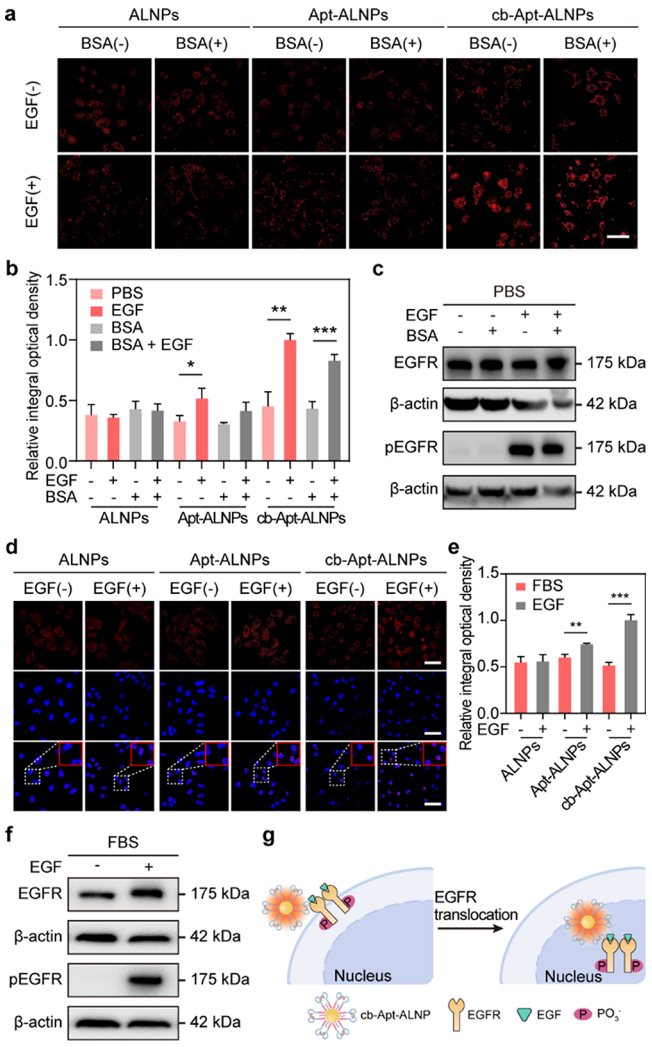

Figure 2. The cb-Apt-ALNPs could image EGFR nuclear translocation in complex biological environments. Representative afterglow images (a) and corresponding relative IOD (b) of ALNPs, Apt-ALNPs, and cb-Apt-ALNPs from A549 cells after different treatments. Scale bar, 50 μm. Data are shown as the mean ± standard deviation. n = 3; *P < 0.1, **P < 0.01, ***P < 0.001, analyzed by two-sided Student's t-test. (c) WB analysis of EGFR and pEGFR in A549 cells with different treatments in PBS. Representative afterglow images, nuclear DAPI staining images (d), and corresponding relative IOD (e) of ALNPs, Apt-ALNPs, and cb-Apt-ALNPs from A549 cells incubated without or with EGF in fetal bovine serum (FBS). Scale bar, 50 μm. Data are shown as the mean ± standard deviation. n = 3; **P < 0.01, ***P < 0.001, analyzed by two-sided Student's t-test. (f) WB analysis of EGFR and pEGFR in A549 cells with different treatments in FBS. (g) Schematic of cb-Apt-ALNPs detecting EGFR nuclear translocation in the presence of EGF.

EGFR phosphorylation-inactivated group (Figure 2e). These data highlighted that afterglow imaging monitored by cb-Apt-ALNPs allowed for selective visualization of EGFR nuclear translocation with superior specificity over ALNPs and Apt-ALNPs. Hence, it can be concluded that cb-Apt-ALNPs were capable of visualizing cellular EGFR nuclear translocation status selectively in a complex environment, consistent with the results of WB (Figure 2f and Figure S31). Additionally, the EGFR high-expressing cell line human tongue squamous cell carcinoma (CAL-27) was chosen to investigate the applicability of the cb-Apt-ALNPs (Figure S32).[42,43] For EGF-stimulated CAL-27 cells, the cb-Apt-ALNPs showed a bright afterglow signal. This observation was similar to the signal trend of A549 cells (Figure S33). These phenomena may be due to the fact that EGF activates EGFR phosphorylation, and EGFR carrying luminescent cb-Apt-ALNPs translocates into the nucleus, where they aggregate with bright signals in the nucleus (Figure 2g). These data provided direct evidence supporting that cb-Apt-ALNPs can realize long-term EGFR nuclear translocation imaging with high stability in complex biological environments.

In Situ Imaging the Nuclear Translocation of EGFR. It has been confirmed that cb-Apt-ALNPs possess excellent stability in different biological environments, suggesting that cb-Apt-ALNPs are potential probes for long-term monitoring of nuclear EGFR distribution. To determine whether cb-Apt-ALNPs can monitor the nuclear translocation of EGFR, A549 cells and normal human liver cell line (L02) were incubated with cb-Apt-ALNPs. Then, the cells were imaged along the Z-axis at various depths. The typical cross-section images showed that in the nucleus of A549 cells, the afterglow signal was significantly enhanced after EGF stimulation (Figure 3a and Figure S34). The pseudo-color image at a distance of 1.56 μm on the Z-axis visually presented this observation, indicating that EGFR nuclear translocation was continuously occurring in cancer cells. In addition, the EGFR nuclear translocation exhibited an EGF-dependent increase, which was confirmed by the fluorescence profile of the indicated region (white line). For L02 cells, the nucleus showed a near-zero signal with and without EGF pretreatment (Figure 3b and Figure S35), elucidating a low degree of EGFR nuclear translocation in the normal cells. Using nuclear fractionation and WB, it was found that the bands for EGFR (Figure 3c) and pEGFR (Figure 3d) were more clearly displayed in the nucleus of A549 cells than L02 cells after EGF stimulation, highly consistent with the results of Z-axis scanning. Furthermore, temporal dynamic signal changes of cb-Apt-ALNPs during EGFR translocation were also examined. The observations suggested that cb-Apt-ALNPs had a temporal dynamic response to EGFR nuclear translocation for nearly an hour (Figures S36 and S37). These phenomena demonstrated that the distribution of EGFR in the nucleus of living cells can be monitored by the signal of cb-Apt-ALNPs, enabling the differentiation of cancer cells from normal cells.

Visualization of EGFR Nuclear Translocation in Migrated Cells. It has been reported that EGF stimulation can induce EGFR phosphorylation and promote EGFR translocation to the nucleus in tumor cells.[4] By binding to genes in the nucleus, EGFR regulates gene transcription and stimulates the expression of cyclin D1, leading to tumor cell migration.[44] We further investigated whether cb-Apt-ALNPs could monitor EGFR nuclear translocation in cells with strong migration ability. The optical signals of cb-Apt-ALNPs during cell migration were observed by confocal laser microscopy. From the photographs of migration, the migration rate of A549 cells pretreated with EGF was faster than that of L02 cells (Figure 4a). Statistical analysis and WB results illustrated that EGF can promote EGFR translocation to the nucleus, and the scratch area of A549 cells decreased to nearly 20% after 48 h, showing strong migration ability (Figures S38–S40). Then, the cb-Apt-ALNPs were incubated with A549 cells and L02 cells. The afterglow luminescence of the nucleus in A549 cells was significantly enhanced after EGF stimulation (Figure 4b). The luminescence intensity of cb-Apt-ALNPs was highly

https://doi.org/10.1021/acs.analchem.2c02762
Anal. Chem. XXXX, XXX, XXX−XXX

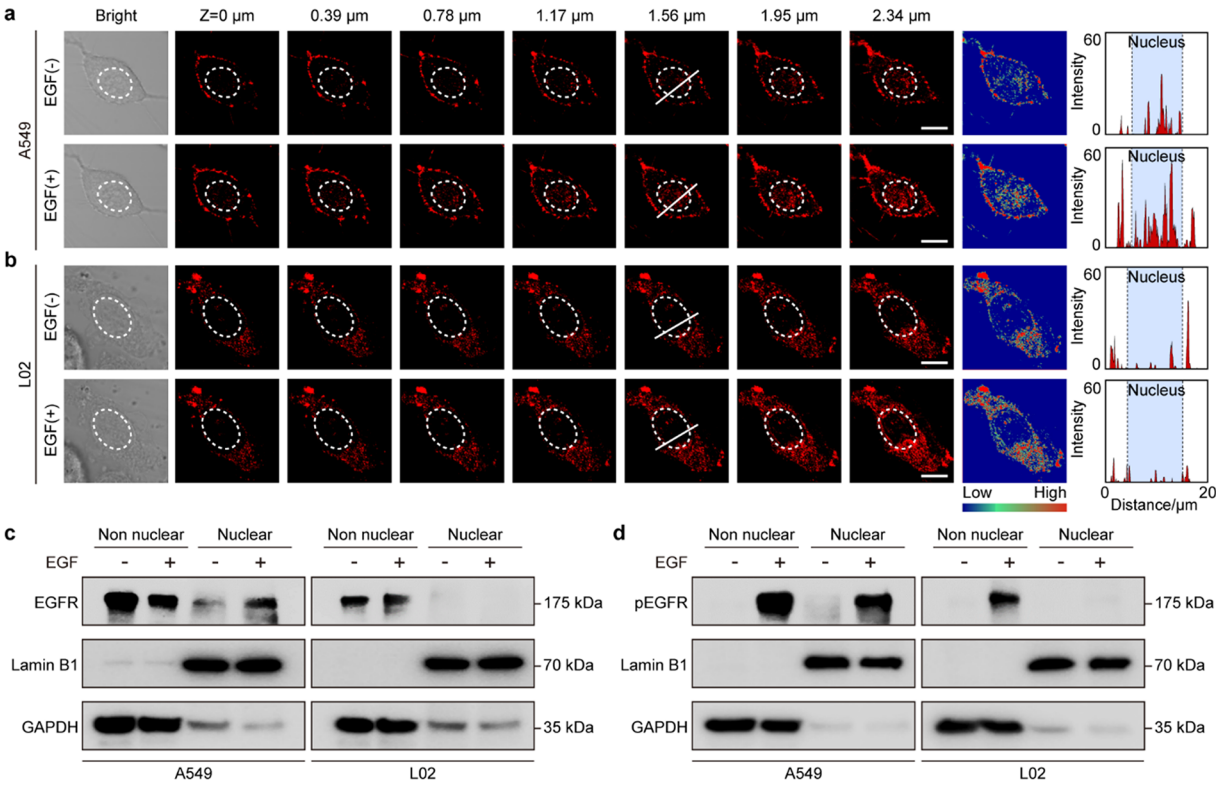

Figure 3. *Z*-Axis scanning images of internalized cb-Apt-ALNPs in A549 cells (a) and L02 cells (b) were recorded by a confocal microscope before or after EGF stimulation. Micrographs were taken as the focal plane gradually moved from the bottom to the top of the cell. Scale bar, 10 μm. From left to right: brightfield image at the *Z*-axis distance of 1.56 μm, *Z*-axis scanning images (the white dotted line represents the boundary of the nucleus), pseudo-color image at the *Z*-axis distance of 1.56 μm, and fluorescence profiling of the white solid line (the light blue area represents the nuclear region; the white area represents the cytoplasmic region). WB analysis of EGFR (c) and pEGFR (d) in non-nuclear and nuclear proteins of A549 cells and L02 cells stimulated with EGF. Lamin B1 and GAPDH were used as purity controls for the nuclear and non-nuclear proteins, respectively.

consistent with the degree of cell migration, suggesting that monitoring the nuclear translocation signal of intracellular EGFR can be used for tumor status evaluation. To further explore the imaging of EGFR nuclear translocation by cb-Apt-ALNPs in tumor tissues, the performance of cb-Apt-ALNPs was evaluated by the 3D multicellular spheroid (MCS) model with histological features similar to the solid tumor. In the presence of EGF, the afterglow image obtained in A549 MCSs exhibited significant brightness throughout the spheroid. In sharp contrast, for L02 MCSs, only the edge of the spheroids showed dim afterglow, while the inner region near the center was almost as dark as the background (Figure 4c). Such afterglow imaging of the MCSs models clearly demonstrated the ability of cb-Apt-ALNPs to in situ monitor EGFR nuclear translocation in tumor tissues (Figure 4d), explicitly indicating their superiority for imaging EGFR nuclear translocation.

Imaging of EGFR Nuclear Translocation in Mice. It is reported that EGFR nuclear translocation at tumor sites remains active to meet the needs of proliferation and migration during tumor growth (Figure 5a).[45] Consequently, monitoring EGFR nuclear translocation *in vivo* can not only assess the growth status of cancer cells but also show the malignant degree of tumors. Encouraged by the good results obtained in tumor tissues, A549 tumor-bearing mice were used as a murine model to further clarify the real-time monitoring capability of cb-Apt-ALNPs for EGFR nuclear translocation. The biosafety of cb-Apt-ALNPs was evaluated by measuring their tissue and blood compatibilities in healthy BALB/c mice. The body weight of mice was monitored for 14 days after treatment, and no apparent body weight loss was observed (Figure S41). Compared with the PBS-treated group, the cb-Apt-ALNPs-treated group displayed no significant differences in both hematology parameters and blood biochemical indexes (Figures S42−S45). The results manifested the excellent biocompatibility of cb-Apt-ALNPs in the mice model, laying a solid foundation for further *in vivo* application. Cetuximab, as an EGFR inhibitor, was used to inhibit EGFR nuclear translocation by blocking the binding of EGFR and its ligand.[46] The mice receiving inhibitor-treated or inhibitor-untreated were imaged by cb-Apt-ALNPs. Also, the biodistribution of cb-Apt-ALNPs in mice were tracked using the *in vivo* imaging system. As shown in Figure 5b,c, in the inhibitor-untreated group, the afterglow intensity at the tumor site was strong, manifesting that the EGFR nuclear translocation was active. However, in the inhibited group, the afterglow intensity at the tumor site gradually weakened with the treatment of the inhibitor. Notably, 24 h after probe injection, the afterglow signal in the tumor of the uninhibited mice was still clearly visible, illustrating excellent long-term stability of the probe *in vivo*. The cb-Apt-ALNPs displayed tumor accumulation (Figures S46−S48), and showed negligible neurotoxicity (Figure S49). The results suggested that the afterglow signal of cb-Apt-ALNPs can dynamically reflect the entire process of EGFR nuclear translocation in mice.

The expressions of EGFR and pEGFR in tumor tissues were detected by traditional immunohistochemistry (IHC). There

https://doi.org/10.1021/acs.analchem.2c02762
Anal. Chem. XXXX, XXX, XXX−XXX

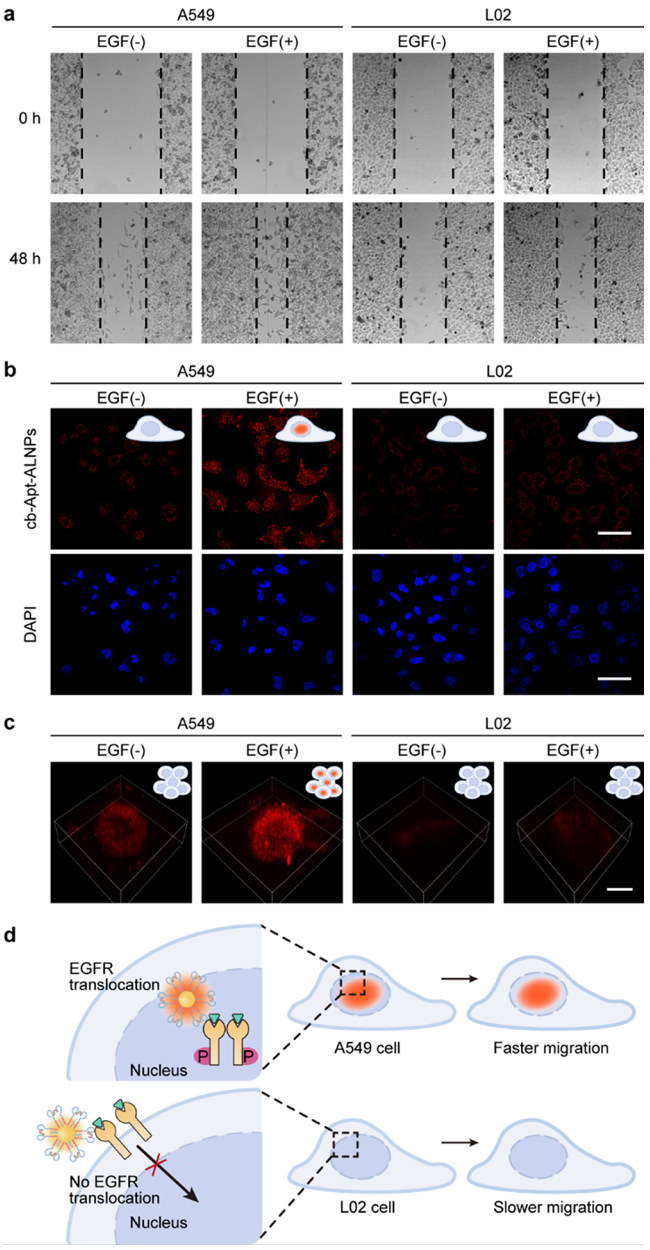

Figure 4. Evaluation of the cb-Apt-ALNPs for imaging of EGFR nuclear translocation in migrated cells. (a) Cell migration results. The black dotted lines define the area lacking cells. (b) Representative afterglow images and corresponding nuclear DAPI staining images of A549 cells and L02 cells after incubation cb-Apt-ALNPs without or with EGF. Scale bar, 50 μm. (c) 3D images of A549 MCSs and L02 MCSs after incubation cb-Apt-ALNPs without or with EGF. Scale bar, 200 μm. (d) Schematic of the relationship between the afterglow signal of cb-Apt-ALNPs and cell migration.

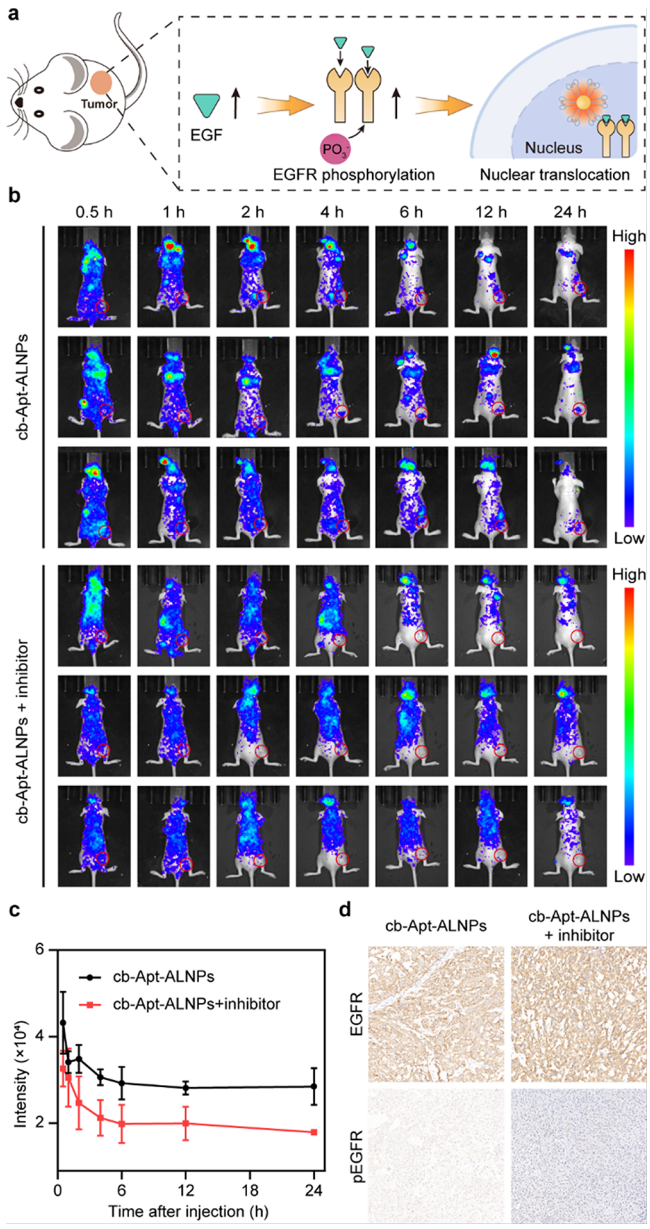

Figure 5. Evaluation of the cb-Apt-ALNPs for *in vivo* imaging of EGFR nuclear translocation. (a) Illustration of EGFR nuclear translocation at tumor sites in mice. (b) Time-dependent afterglow images of the A549 tumor-bearing mice treated with or without inhibitor after intravenous injection of cb-Apt-ALNPs. The red circles represent the boundary of the tumor. n = 3. Color scale: 2.75×10^3–1.5×10^4. (c) Quantitative analysis of afterglow intensity in tumor region of mice shown in (b). Data are shown as the mean ± standard deviation. n = 3. (d) IHC staining of EGFR and pEGFR in tissue sections of mice injected with or without inhibitor.

was almost no difference in EGFR expression of tumor tissues treated with or without inhibitor. The tumor tissue from the inhibitor-treated group exhibited a weaker brown signal of pEGFR compared to the untreated group (Figure 5d and Figure S50), confirming the low expression of pEGFR. The downregulation of pEGFR further revealed that EGFR phosphorylation activity was inhibited after adding inhibitor, and the nuclear translocation of EGFR was attenuated. In addition, the Ki67 assay and terminal deoxynucleotidyl transferase (TdT)-mediated dUTP nick-end labeling (TUNEL) assay were employed to evaluate the levels of proliferation and apoptosis in tumor tissues to analyze the tumor suppression efficiency. In short, the tumor tissue from inhibitor-treated mice displayed higher apoptosis and lower proliferation levels compared to the untreated group (Figures S51 and S52). The inhibitor attenuates the level of nuclear translocation of EGFR, matching well with the accepted view that EGFR nuclear translocation occurs rarely in growth-retarded tumor cells. Collectively, EGFR nuclear translocation occurred frequently in tumor cells and displayed bright afterglow signals while rarely in suppressed tumor cells. In

https://doi.org/10.1021/acs.analchem.2c02762
Anal. Chem. XXXX, XXX, XXX−XXX

general, monitoring EGFR nuclear translocation can be used to evaluate tumor status in mice and may lead to new strategies for detecting the occurrence and progression of related diseases.

CONCLUSIONS

In this work, cb-Apt-ALNPs were designed for long-term stable detection of EGFR nuclear translocation in situ. On the basis of targeting EGFR, the probe could respond to EGFR phosphorylation in the first step and realize in situ monitoring EGFR nuclear translocation in the second step. The cb-Apt-ALNPs were able to maintain stability for up to 8 h in serum and up to 12 h in the Exo I environment, laying the foundation for nuclear translocation monitoring. Cellular experimental results demonstrated that cb-Apt-ALNPs exhibited sensitive responses to EGFR nuclear translocation triggered by EGF at a concentration of 2 $\mu g \cdot mL^{-1}$. The tissue and *in vivo* experimental results indicated that the afterglow signal of cb-Apt-ALNPs could sustainedly reflect the status of EGFR nuclear translocation for up to 1 h. Thus, cb-Apt-ALNPs could be used to detect the biological progress of EGFR nuclear translocation in situ. Overall, cb-Apt-ALNPs enable long-term stable EGFR nuclear translocation detection, presenting a promising strategy for assessing tumor status. Furthermore, the cb-Apt-ALNPs probe can easily be extended to detect EGFR nuclear translocation in other tumor cell lines such as CAL-27. The probes based on cb-Apt-ALNPs can form a robust and versatile toolbox for creating comprehensive detection of related diseases.

ASSOCIATED CONTENT

Supporting Information

The Supporting Information is available free of charge at https://pubs.acs.org/doi/10.1021/acs.analchem.2c02762.

Reagents and materials, sample characterization, experimental section, and supplementary figures (PDF)

AUTHOR INFORMATION

Corresponding Author

Jie Tan − *Molecular Science and Biomedicine Laboratory (MBL), State Key Laboratory of Chemo/Biosensing and Chemometrics, College of Chemistry and Chemical Engineering, Hunan University, Changsha 410082, China*; Email: tanjie0416@hnu.edu.cn

Authors

Lei Zhang − *Molecular Science and Biomedicine Laboratory (MBL), State Key Laboratory of Chemo/Biosensing and Chemometrics, College of Chemistry and Chemical Engineering, Hunan University, Changsha 410082, China*

Mengge Chu − *Molecular Science and Biomedicine Laboratory (MBL), State Key Laboratory of Chemo/Biosensing and Chemometrics, College of Chemistry and Chemical Engineering, Hunan University, Changsha 410082, China*

Cailing Ji − *Molecular Science and Biomedicine Laboratory (MBL), State Key Laboratory of Chemo/Biosensing and Chemometrics, College of Chemistry and Chemical Engineering, Hunan University, Changsha 410082, China*

Junyuan Wei − *Molecular Science and Biomedicine Laboratory (MBL), State Key Laboratory of Chemo/Biosensing and Chemometrics, College of Chemistry and Chemical Engineering, Hunan University, Changsha 410082, China*

Yanbing Yang − *College of Chemistry and Molecular Sciences, Wuhan University, Wuhan 430072, China*

Zhongnan Huang − *Molecular Science and Biomedicine Laboratory (MBL), State Key Laboratory of Chemo/Biosensing and Chemometrics, College of Chemistry and Chemical Engineering, Hunan University, Changsha 410082, China*

Weihong Tan − *Molecular Science and Biomedicine Laboratory (MBL), State Key Laboratory of Chemo/Biosensing and Chemometrics, College of Chemistry and Chemical Engineering, Hunan University, Changsha 410082, China; The Cancer Hospital of the University of Chinese Academy of Sciences (Zhejiang Cancer Hospital), Hangzhou Institute of Medicine (HIM), Chinese Academy of Sciences, Hangzhou, Zhejiang 310022, China; Institute of Molecular Medicine (IMM), Renji Hospital, Shanghai Jiao Tong University School of Medicine, and College of Chemistry and Chemical Engineering, Shanghai Jiao Tong University, Shanghai 200240, China*; orcid.org/0000-0002-8066-1524

Quan Yuan − *Molecular Science and Biomedicine Laboratory (MBL), State Key Laboratory of Chemo/Biosensing and Chemometrics, College of Chemistry and Chemical Engineering, Hunan University, Changsha 410082, China; College of Chemistry and Molecular Sciences, Wuhan University, Wuhan 430072, China*; orcid.org/0000-0002-3085-431X

Complete contact information is available at: https://pubs.acs.org/10.1021/acs.analchem.2c02762

Author Contributions

The manuscript was written through contributions of all authors.

Notes

The authors declare no competing financial interest.

ACKNOWLEDGMENTS

This work was supported by the National Key R&D Program of China (2017YFA0208000), Natural Science Foundation of Hunan Province (2022JJ20005), and National Natural Science Foundation of China (22174038, 21925401, 21904037), and Tencent Foundation.

REFERENCES

(1) Kau, T. R.; Silver, P. A. *Drug Discovery Today* **2003**, *8*, 78−85.
(2) Kim, S. B.; Ozawa, T.; Watanabe, S.; Umezawa, Y. *Proc. Natl. Acad. Sci. U. S. A.* **2004**, *101*, 11542−11547.
(3) Kau, T. R.; Way, J. C.; Silver, P. A. *Nat. Rev. Cancer* **2004**, *4*, 106−117.
(4) Lin, S.-Y.; Makino, K.; Xia, W.; Matin, A.; Wen, Y.; Kwong, K. Y.; Bourguignon, L.; Hung, M.-C. *Nat. Cell Biol.* **2001**, *3*, 802−808.
(5) Kaplan, M.; Narasimhan, S.; de Heus, C.; Mance, D.; van Doorn, S.; Houben, K.; Popov-Čeleketić, D.; Damman, R.; Katrukha, E. A.; Jain, P.; Geerts, W. J. C.; Heck, A. J. R.; Folkers, G. E.; Kapitein, L. C.; Lemeer, S.; van Bergen En Henegouwen, P. M. P.; Baldus, M. *Cell* **2016**, *167*, 1241−1251.e11.
(6) Begley, M. J.; Yun, C. H.; Gewinner, C. A.; Asara, J. M.; Johnson, J. L.; Coyle, A. J.; Eck, M. J.; Apostolou, I.; Cantley, L. C. *Nat. Struct. Mol. Biol.* **2015**, *22*, 983−990.
(7) Capuani, F.; Conte, A.; Argenzio, E.; Marchetti, L.; Priami, C.; Polo, S.; Di Fiore, P. P.; Sigismund, S.; Ciliberto, A. *Nat. Commun.* **2015**, *6*, 7999−8012.

(8) Kickhoefer, V. A.; Han, M.; Raval-Fernandes, S.; Poderycki, M. J.; Moniz, R. J.; Vaccari, D.; Silvestry, M.; Stewart, P. L.; Kelly, K. A.; Rome, L. H. *ACS Nano* **2009**, *3*, 27−36.
(9) Needham, S. R.; Roberts, S. K.; Arkhipov, A.; Mysore, V. P.; Tynan, C. J.; Zanetti-Domingues, L. C.; Kim, E. T.; Losasso, V.; Korovesis, D.; Hirsch, M.; Rolfe, D. J.; Clarke, D. T.; Winn, M. D.; Lajevardipour, A.; Clayton, A. H.; Pike, L. J.; Perani, M.; Parker, P. J.; Shan, Y.; Shaw, D. E.; Martin-Fernandez, M. L. *Nat. Commun.* **2016**, *7*, 13307−13320.
(10) Al-Akhrass, H.; Naves, T.; Vincent, F.; Magnaudeix, A.; Durand, K.; Bertin, F.; Melloni, B.; Jauberteau, M. O.; Lalloué, F. *Nat. Commun.* **2017**, *8*, 1182−1196.
(11) Pal, R.; Kang, H.; Choi, H. S.; Kumar, A. T. N. *Clin. Cancer Res.* **2019**, *25*, 6653−6661.
(12) Sako, Y.; Minoghchi, S.; Yanagida, T. *Nat. Cell Biol.* **2000**, *2*, 168−172.
(13) Delcanale, P.; Porciani, D.; Pujals, S.; Jurkevich, A.; Chetrusca, A.; Tawiah, K. D.; Burke, D. H.; Albertazzi, L. *Angew. Chem., Int. Ed.* **2020**, *59*, 18546−18555.
(14) Yan, Q.; Cai, M.; Zhou, L.; Xu, H.; Shi, Y.; Sun, J.; Jiang, J.; Gao, J.; Wang, H. *Nanoscale Adv.* **2019**, *1*, 291−298.
(15) Opazo, F.; Levy, M.; Byrom, M.; Schäfer, C.; Geisler, C.; Groemer, T. W.; Ellington, A. D.; Rizzoli, S. O. *Nat. Methods* **2012**, *9*, 938−939.
(16) Strauss, S.; Nickels, P. C.; Strauss, M. T.; Jimenez Sabinina, V.; Ellenberg, J.; Carter, J. D.; Gupta, S.; Janjic, N.; Jungmann, R. *Nat. Methods* **2018**, *15*, 685−688.
(17) Bianchi, F.; Sasso, M.; Turdo, F.; Beretta, G. L.; Casalini, P.; Ghirelli, C.; Sfondrini, L.; Ménard, S.; Tagliabue, E.; Campiglio, M. *J. Cell. Physiol.* **2015**, *230*, 2661−2670.
(18) Maik-Rachline, G.; Lifshits, L.; Seger, R. *Int. J. Mol. Sci.* **2020**, *21*, 6102.
(19) Zhou, J.; Rossi, J. *Nat. Rev. Drug Discovery* **2017**, *16*, 181−202.
(20) Keefe, A. D.; Pai, S.; Ellington, A. *Nat. Rev. Drug Discovery* **2010**, *9*, 537−550.
(21) Kuai, H.; Zhao, Z.; Mo, L.; Liu, H.; Hu, X.; Fu, T.; Zhang, X.; Tan, W. *J. Am. Chem. Soc.* **2017**, *139*, 9128−9131.
(22) Hu, J.; Zhao, Z.; Liu, Q.; Ye, M.; Hu, B.; Wang, J.; Tan, W. *Chem. − Asian J.* **2015**, *10*, 1519−1525.
(23) Tan, J.; Li, H.; Hu, X.; Abdullah, R.; Xie, S.; Zhang, L.; Zhao, M.; Luo, Q.; Li, Y.; Sun, Z.; Yuan, Q.; Tan, W. *Chem* **2019**, *5*, 1775−1792.
(24) Wang, J.; Ma, Q.; Zheng, W.; Liu, H.; Yin, C.; Wang, F.; Chen, X.; Yuan, Q.; Tan, W. *ACS Nano* **2017**, *11*, 8185−8191.
(25) Li, J.; Hong, C. Y.; Wu, S. X.; Liang, H.; Wang, L. P.; Huang, G.; Chen, X.; Yang, H. H.; Shangguan, D.; Tan, W. *J. Am. Chem. Soc.* **2015**, *137*, 11210−11213.
(26) Peng, L.; You, M.; Wu, C.; Han, D.; Öçsoy, I.; Chen, T.; Chen, Z.; Tan, W. *ACS Nano* **2014**, *8*, 2555−2561.
(27) Tan, J.; Li, H.; Ji, C.; Zhang, L.; Zhao, C.; Tang, L.; Zhang, C.; Sun, Z.; Tan, W.; Yuan, Q. *Nat. Commun.* **2022**, *13*, 594.
(28) Ji, C.; Tan, J.; Yuan, Q. *Chin. J. Chem.* **2021**, *39*, 3188−3198.
(29) Huang, K.; Le, N.; Wang, J. S.; Huang, L.; Zeng, L.; Xu, W.-C.; Li, Z.; Li, Y.; Han, G. *Adv. Mater.* **2022**, *34*, No. 2107962.
(30) Hai, O.; Yang, E.; Ren, Q.; Wu, X.; Ren, Y.; Zhao, Y.; Zhu, J. *J. Lumin.* **2020**, *220*, No. 116965.
(31) Miao, Q.; Xie, C.; Zhen, X.; Lyu, Y.; Duan, H.; Liu, X.; Jokerst, J. V.; Pu, K. *Nat. Biotechnol.* **2017**, *35*, 1102−1110.
(32) Li, J.; Mohammed-Elsabagh, M.; Paczkowski, F.; Li, Y. *ChemBioChem* **2020**, *21*, 1547−1566.
(33) Cromie, G. A.; Connelly, J. C.; Leach, D. F. *Mol. Cell* **2001**, *8*, 1163−1174.
(34) Ji, D.; Lyu, K.; Zhao, H.; Kwok, C. K. *Nucleic Acids Res.* **2021**, *49*, 7280−7291.
(35) Litke, J. L.; Jaffrey, S. R. *Nat. Biotechnol.* **2019**, *37*, 667−675.
(36) Qian, Y.; Qiu, M.; Wu, Q.; Tian, Y.; Zhang, Y.; Gu, N.; Li, S.; Xu, L.; Yin, R. *Sci. Rep.* **2015**, *4*, 7490.
(37) Li, Z.; Liang, T.; Lv, S.; Zhuang, Q.; Liu, Z. *J. Am. Chem. Soc.* **2015**, *137*, 11179−11185.
(38) Xu, S.; Chen, R.; Zheng, C.; Huang, W. *Adv. Mater.* **2016**, *28*, 9920−9940.
(39) Jones, S.; King, P. J.; Antonescu, C. N.; Sugiyama, M. G.; Bhamra, A.; Surinova, S.; Angelopoulos, N.; Kragh, M.; Pedersen, M. W.; Hartley, J. A.; Futter, C. E.; Hochhauser, D. *Sci. Rep.* **2020**, *10*, 663.
(40) Faria, J. A. Q. A.; de Andrade, C.; Goes, A. M.; Rodrigues, M. A.; Gomes, D. A. *Biochem. Biophys. Res. Commun.* **2016**, *478*, 39−45.
(41) Rubio-Pereda, P.; Vilhena, J. G.; Takeuchi, N.; Serena, P. A.; Pérez, R. *J. Chem. Phys.* **2017**, *146*, 214704.
(42) Orcutt, K. P.; Parsons, A. D.; Sibenaller, Z. A.; Scarbrough, P. M.; Zhu, Y.; Sobhakumari, A.; Wilke, W. W.; Kalen, A. L.; Goswami, P.; Miller, F. J., Jr.; Spitz, D. R.; Simons, A. L. *Cancer Res.* **2011**, *71*, 3932−3940.
(43) Rusnak, D. W.; Alligood, K. J.; Mullin, R. J.; Spehar, G. M.; Arenas-Elliott, C.; Martin, A.-M.; Degenhardt, Y.; Rudolph, S. K.; Haws, T. F., Jr; Hudson-Curtis, B. L.; Gilmer, T. M. *Cell Prolif.* **2007**, *40*, 580−594.
(44) Brand, T. M.; Iida, M.; Li, C.; Wheeler, D. L. *Discov. Med.* **2011**, *12*, 419−432.
(45) Blobel, C. P. *Nat. Rev. Mol. Cell Biol.* **2005**, *6*, 32−43.
(46) Steiner, P.; Joynes, C.; Bassi, R.; Wang, S.; Tonra, J. R.; Hadari, Y. R.; Hicklin, D. J. *Clin. Cancer Res.* **2007**, *13*, 1540−1551.

https://doi.org/10.1021/acs.analchem.2c02762
Anal. Chem. XXXX, XXX, XXX−XXX